



# Structural and Mechanical Properties of Silica Mesoporous Films Synthesized Using Deep X-Rays: Implications in the Construction of Devices

Paula Y. Steinberg<sup>1</sup>, Diego F. Lionello<sup>1,2</sup>, Daiana E. Medone Acosta<sup>1,2,3</sup>, M. Mercedes Zalduendo<sup>1</sup>, Heinz Amenitsch<sup>4</sup>, Leticia P. Granja<sup>3,5</sup>, Benedetta Marmiroli<sup>4</sup>, Paula C. Angelomé<sup>1,5\*</sup> and M. Cecilia Fuertes<sup>1,5\*</sup>

<sup>1</sup>Gerencia Química, Centro Atómico Constituyentes, Comisión Nacional de Energía Atómica, San Martín, Argentina, <sup>2</sup>Instituto Sabato, Comisión Nacional de Energía Atómica – Universidad Nacional de San Martín, San Martín, Argentina, <sup>3</sup>Departamento de Física de la Materia Condensada, Gerencia de Investigación y Aplicaciones, Centro Atómico Constituyentes, Comisión Nacional de Energía Atómica, San Martín, Argentina, <sup>4</sup>Institute of Inorganic Chemistry, Graz University of Technology, Graz, Austria, <sup>5</sup>Instituto de Nanociencia y Nanotecnología, CONICET-CNEA, San Martín, Argentina

## OPEN ACCESS

### Edited by:

P. Davide Cozzoli,  
University of Salento, Italy

### Reviewed by:

Hyung-Ho Park,  
Yonsei University, South Korea  
Zhangxiong Wu,  
Soochow University, China  
Luca Malfatti,  
University of Sassari, Italy

### \*Correspondence:

M. Cecilia Fuertes  
mfuertes@cnea.gov.ar  
Paula C. Angelomé  
angelome@cnea.gov.ar

### Specialty section:

This article was submitted to  
Colloidal Materials and Interfaces,  
a section of the journal  
Frontiers in Materials

**Received:** 11 November 2020

**Accepted:** 19 January 2021

**Published:** 19 February 2021

### Citation:

Steinberg PY, Lionello DF, Medone Acosta DE, Zalduendo MM, Amenitsch H, Granja LP, Marmiroli B, Angelomé PC and Fuertes MC (2021) Structural and Mechanical Properties of Silica Mesoporous Films Synthesized Using Deep X-Rays: Implications in the Construction of Devices. *Front. Mater.* 8:628245. doi: 10.3389/fmats.2021.628245

In recent years, the use of X-Rays (XR) irradiation for the production of ordered mesoporous thin films has been well established. This technique allows obtaining porous materials that contain thermal sensitive moieties or nanoparticles. Additionally, in combination with lithographic masks, the generation of high aspect ratio patterns of several geometrical shapes with micrometric resolution is possible. In this work, the structural and mechanical properties of porous silica thin films obtained by sol-gel method along with the exposure to high intensity XR is presented. Two templates (CTAB and Brij 58) and several irradiation doses and post-synthesis treatments were evaluated by a combination of characterization techniques, including grazing incidence small-angle XR scattering, electronic microscopies, XR reflectometry and nanoindentation. The results demonstrate that all the irradiated oxides presented a highly ordered mesoporous structure, independently of the XR dose and post thermal treatment. Their mechanical properties, on the other hand, clearly depend on the irradiation dose; high hardness values were measured on samples irradiated at low doses but higher doses are necessary to obtain films with indentation modulus values similar to the obtained for thermally treated coatings. The accessible porosity, essential for the application of these films in devices for micro- and nanofluidics, is also dependent on the dose and the thermal treatment performed afterward. The same tendency is observed for the films contraction and rigidity. After this characterization, it was concluded that thermal treatments are needed after the consolidation with XR to increase the accessibility and structural integrity of these porous oxides. Finally, the production of composites with metallic (Au and Ag) nanoparticles was tested which envisioned their applications in sensing and catalysis. Moreover, diverse geometrical patterns of both pure and Ag nanoparticles doped silica mesostructured films were obtained, demonstrating the feasibility of the proposed approach. The results presented in this work are of great importance to

understand the transport mechanisms that operate in these silica porous films, in order to integrate them in different devices for lab-on-a-chip applications.

**Keywords:** mesoporous thin films, deep x-ray lithography, silica, mechanical properties, metallic nanoparticles

## INTRODUCTION

Mesoporous oxides, and particularly silica ones, have been widely studied in the last years for transport related applications mainly due to their high surface-volume ratio and their ordered porous structure, which allows the rapid diffusion of analytes. One approach to exploit their capabilities is through the synthesis of mesoporous oxides in the form of thin films, enabling their implementation in microfabrication techniques in order to be integrated into complex functional devices. The combined properties of a highly controlled porous system and those inherent to a thin film make these materials attractive for being included in several devices, from sensors to supercapacitors or biological devices (Innocenzi and Malfatti, 2013).

Mesoporous oxide thin films are usually synthesized using the sol-gel method in combination with the self-assembly of a surfactant (Brinker et al., 1999; Grosso et al., 2004; Sánchez et al., 2008). After the synthesis, two procedures can be used to consolidate the inorganic walls and remove the organic template to originate the porous structure: 1) thermal treatments at moderate temperature (300–500°C) (Grosso et al., 2000; Soler-Illia et al., 2012; Lionello et al., 2017); 2) a low temperature (130–200°C) thermal treatment followed by template elimination using chemical dissolution in a proper solvent (Escobar et al., 2017; Gonzalez Solveyra et al., 2017; Giménez et al., 2020). In these two cases, the contraction of the films in the direction perpendicular to the substrate promotes the interconnection of the pores, which generates the accessible mesoporosity; this feature is usually required for the integration of these films in functional devices. After synthesis and consolidation of the mesoporous films, their accessible pores can be filled with different species (solvents, organic molecules, nanoparticles, etc.) to tune their final properties and expand the application fields (Angelomé and Liz-Marzán, 2014; Wolosiuk et al., 2014; Angelomé and Fuertes, 2018). The films accessible porosity gives material scientists the possibility to incorporate new functional features but also affects the structural and mechanical properties of the oxides (Xiao et al., 2003; Fan et al., 2007). In general, an increase in porosity leads to a reduction in elastic modulus and hardness; this issue represents a challenge to be addressed in the field of thin films nanomechanics (Dubois et al., 2008; Zhou et al., 2011; Vanstreels et al., 2012).

More recently, the use of hard XR as an alternative treatment to thermal consolidation for the production of ordered mesoporous films has been established (Innocenzi et al., 2012; Innocenzi et al., 2014). The XR irradiation of sol-gel materials has been successfully used to obtain porous oxides (mainly titania and silica) that could contain thermal sensitive moieties (Falcaro et al., 2009; Falcaro et al., 2011; Doherty et al., 2012) or

nanoparticles (Malfatti et al., 2010; Malfatti et al., 2011; Pinna et al., 2013; Malfatti et al., 2016). In almost all reported cases, the triblock copolymer Pluronic F127 was employed as structure directing agent and thus all the obtained oxides presented the same interpore distance (*ca.* 12 nm) and pore array (cubic *Im3m*).

Moreover, this technique of processing soft matter provides the possibility to generate complex patterns and objects (extruded in the direction perpendicular to the substrate) by the combination of XR with lithographic masks (Marmioli and Amenitsch, 2012). This procedure, named deep X-Ray lithography (DXRL), which generally employs synchrotron radiation as light source, produces the patterns in a single step, avoiding some typical problems associated with the conventional microfabrication techniques, as photoresine wastes and developing artifacts. Furthermore, DXRL presents some other advantages over the existing microfabrication technologies: very high aspect ratio (greater than 100), lateral resolution limit in the nanoscale, and high penetration lengths, which ensures an efficient patterning of thick films (Cerrina, 2000; Costacurta et al., 2010; Falcaro et al., 2011; Innocenzi et al., 2012). DXRL specific capabilities could be exploited in device production in several fields of nanoscience such as sensing, electronics, biology, microfluidics, data storage, and electrochemistry. In fact, mesoporous films and nanocomposite materials based on porous silica have already been fabricated using this patterning technique for applications as surface-enhanced Raman spectroscopy (SERS) platforms (Malfatti et al., 2011), bioactive substrates (Doherty et al., 2012) and lab-on-a-chip devices (Falcaro et al., 2008).

The exposition to hard XR is indeed not only a lithographic process but also could be used as a tool for manipulating the materials properties (Innocenzi et al., 2014). It is well established in the literature that the exposure of the sol-gel films to hard XR produces the densification of the oxide and the partial decomposition of the surfactant and other organic components in the case of hybrids films (Innocenzi et al., 2011; Innocenzi et al., 2012). However, the accessible porosity and stiffness of these irradiated films has not been evaluated in previous works. These properties are of great interest for the application of silica mesoporous platforms in devices for nano and microfluidics, in which the transport of fluids and the film stability in different solvents are of vital importance.

The aim of this work is to evaluate and correlate the consolidation, contraction, accessible porosity and mechanical properties of mesoporous silica films synthesized by high intensity XR irradiation. Two templates were used to generate the pore structure in silica films: the diblock copolymer Brij 58 and the cationic surfactant CTAB, which reproducibly generate a highly accessible mesoporosity in the case of thermally treated films (Etienne et al., 2007; Fuertes et al., 2008). Interestingly, the use of these templates allows obtaining mesostructured silica

films with smaller pore sizes and different pore arrays, in comparison with the previously reported Pluronic F127 templated oxides. As a consequence, changes in their properties and expanding in their potential applications can be expected.

The structural and mechanical properties of the irradiated films were studied using several techniques, including electronic microscopy, infrared spectroscopy, ellipsometry, small-angle XR scattering, XR reflectometry and nanoindentation. The effect of the irradiation dose, the removal of the surfactant with ethanol and post-thermal treatments was assessed.

Finally, the one-step production of patterned mesoporous films based on metallic nanoparticles and silica composites was evaluated, with promising results.

## MATERIALS AND METHODS

### Synthesis

Mesoporous SiO<sub>2</sub> thin films were synthesized by combining sol-gel chemistry and evaporation induced self-assembly (EISA) approach. Tetraethoxysilane (TEOS, Merck) was used as silica precursor. Two surfactants were used to generate the mesoporous structure: cetyltrimethylammonium bromide (CTAB, Sigma Aldrich) and C<sub>16</sub>H<sub>33</sub>(EO)<sub>20</sub>OH (EO = ethylene oxide, Brij 58, Sigma). For the first template, TEOS was first hydrolyzed by refluxing for 1 h in a water/ethanol solution, with molar ratios [H<sub>2</sub>O]:[Si] = 1 and [EtOH]:[Si] = 3. Afterward, CTAB, ethanol (EtOH, BIOPACK) and HCl aqueous solution were added to a final molar composition of 1 TEOS: 20 EtOH: 5 H<sub>2</sub>O: 0.004 HCl: 0.1 CTAB. The solution was aged under stirring at room temperature for at least 72 h before its use (Angelomé et al., 2006). In the case of Brij 58 template, sol was prepared by the direct mixture of the template with TEOS, EtOH and aqueous solution of HCl until a final molar ratio of 1 TEOS: 24 EtOH: 5.2 H<sub>2</sub>O: 0.28 HCl: 0.05 Brij 58 (Liu et al., 2003). This solution was used without aging treatment. The same sol was used to grow metallic nanoparticles inside the films. For the case of Au nanoparticles, a HAuCl<sub>4</sub> (Sigma-Aldrich) solution was directly added to the sol until a final Au:Si molar relation of  $3.7 \times 10^{-3}$  was reached (Malfatti et al., 2010). For Ag nanoparticles, HNO<sub>3</sub> was used instead of HCl (to avoid AgCl precipitation) for the sol preparation; solid AgNO<sub>3</sub> (Sigma-Aldrich) was added to obtain a Ag:Si molar relation of  $8 \times 10^{-2}$ .

Films were deposited on  $20 \times 20 \text{ mm}^2$  silicon or fused silica substrates by spin-coating, at 2000 rpm. Substrates were cleaned with ethanol before film deposition. In selected cases, fused silica substrates with Au nanotriangles (Scarabelli et al., 2014) or Au nanorods (Scarabelli et al., 2015) chemically attached by means of aminopropyltriethoxysilane (Sigma-Aldrich) conjugation were used as substrates (Angelomé and Liz-Marzán, 2010).

As-cast films were directly exposed to hard XR in the DXRL beamline at Elettra Synchrotron facility (Trieste, Italy) (Pérennès et al., 2001). The energy per unit area incident to the sample surface was varied from 34 to 2176 J.cm<sup>-2</sup> by adjusting the exposition time, ranging from a few minutes up to a couple of hours. Some selected samples were irradiated at 14566 J.cm<sup>-2</sup>.

**TABLE 1** | List of samples generated using XR irradiation and/or thermal treatments. X = C for CTAB templated films, and X = B for Brij 58 templated films. d = XR dose (J.cm<sup>-2</sup>).

Sample	XR dose (J.cm <sup>-2</sup> )	Thermal treatment
SX-0	0	—
SX-34	34	—
SX-68	68	—
SX-136	136	—
SX-272	272	—
SX-544	544	—
SX-1088	1088	—
SX-2176	2176	—
SB(Au)-2176	2176	—
SB(Ag)-68	68	—
SB(Ag)-544	544	—
SX-200°C	—	30 min at 200°C
SX-300°C	—	2 h at 300°C
SB-d-200°C	d = 68; 136	30 min at 200°C
SB-d-300°C	d = 68; 136; 272; 2176	2 h at 300°C

The storage ring energy used was 2 GeV, and the XR beam energy range from 2 to 20 KeV. Samples were fixed to a water-cooled mobile stainless steel plate so an area larger than the beam section could be exposed by rastering the sample in front of the beam (Malfatti et al., 2011; Pinna et al., 2013). The maximum exposure area achievable with this system is 80 (width) per 60 (height) mm<sup>2</sup>; therefore the whole  $20 \times 20 \text{ mm}^2$  area of the samples was irradiated.

XR-consolidated films were labeled SX-d, where X = C for CTAB or B for Brij 58, and d is the XR dose in J.cm<sup>-2</sup>. When Ag or Au salts were included to form metallic nanoparticles, the samples were labeled as SB(Ag)-d or SB(Au)-d.

For patterning evaluation, a mask containing test patterns of different sizes, shapes and geometries was used. The mask has a 20 μm-thick gold XR absorber and a 2.2 μm-thick titanium transparent membrane. Immediately after exposure, the samples were developed by immersion in a mixture of the same volumes of water and absolute ethanol for 10 min, so that the unexposed regions of the films were dissolved.

Thermally treated samples were also prepared for comparison purposes. After deposition, the films were consolidated at 60°C for 30 min, then at 130°C for 30 min, and finally treated for 30 min at 200°C. These set of progressive thermal treatments assure the consolidation of the silica matrix but it does not remove the surfactant completely (Angelomé et al., 2006; Fuertes et al., 2007). An additional thermal treatment at 300°C for 2 h was performed in some cases, with a ramp of 1°C min<sup>-1</sup>. These treatments thermally degrade the two studied surfactants. Samples treated at 200°C (or 300°C) were named SX-200°C (or 300°C) or SX-d-200°C (or 300°C) if they received XR irradiation prior to thermal treatment.

The synthesized samples are summarized in **Table 1**.

### Characterization

Fourier transformed Infrared (FTIR) measurements were performed on a Nicolet Magna 560 instrument, equipped with a liquid nitrogen cooled MCT-A detector. FTIR spectra were

acquired using a transmittance arrangement where the films were placed perpendicular to the infrared beam incidence.

Transmission electron microscopy (TEM) images were obtained with a Philips CM 200 electron microscope. Films were scratched from the substrate and deposited on carbon-coated copper grids.

Grazing-incidence small-angle X-ray scattering (GI-SAXS) patterns were acquired at the Austrian SAXS beamline of Elettra Synchrotron (Trieste, Italy), using a 1.54 Å (8 KeV) incidence X-ray beam (Amenitsch et al., 1997). Sample to detector (Pilatus 1M) distance was fixed at 82.49 cm. Silver behenate was used as reference for distance calculations. From GI-SAXS patterns, the pore array of the obtained samples can be determined by comparison with previously reported patterns. The contraction of the pore array, which only occurs in the direction perpendicular to the substrate, was calculated by determining the percentage of deviation from the semicircle in which the first zone of the diffraction patterns area is inscribed in as-prepared films.

Optical images of the samples were obtained using a Leica MZ 125 Microscope.

UV-vis spectra were recorded using either an Ocean Optics spectrophotometer, operating with a DH-2000-BAL deuterium and halogen lamps, and a QEPro CCD spectrometer, or a HP Agilent 8453 spectrophotometer.

Film thicknesses were measured using a spectroscopic ellipsometer HORIBA Auto SE (spectral range 440–1,000 nm and spot size 100 × 100 μm<sup>2</sup>). Ellipsometric data were fitted using Cauchy dielectric model and reported thicknesses were calculated averaging five measurements on each sample.

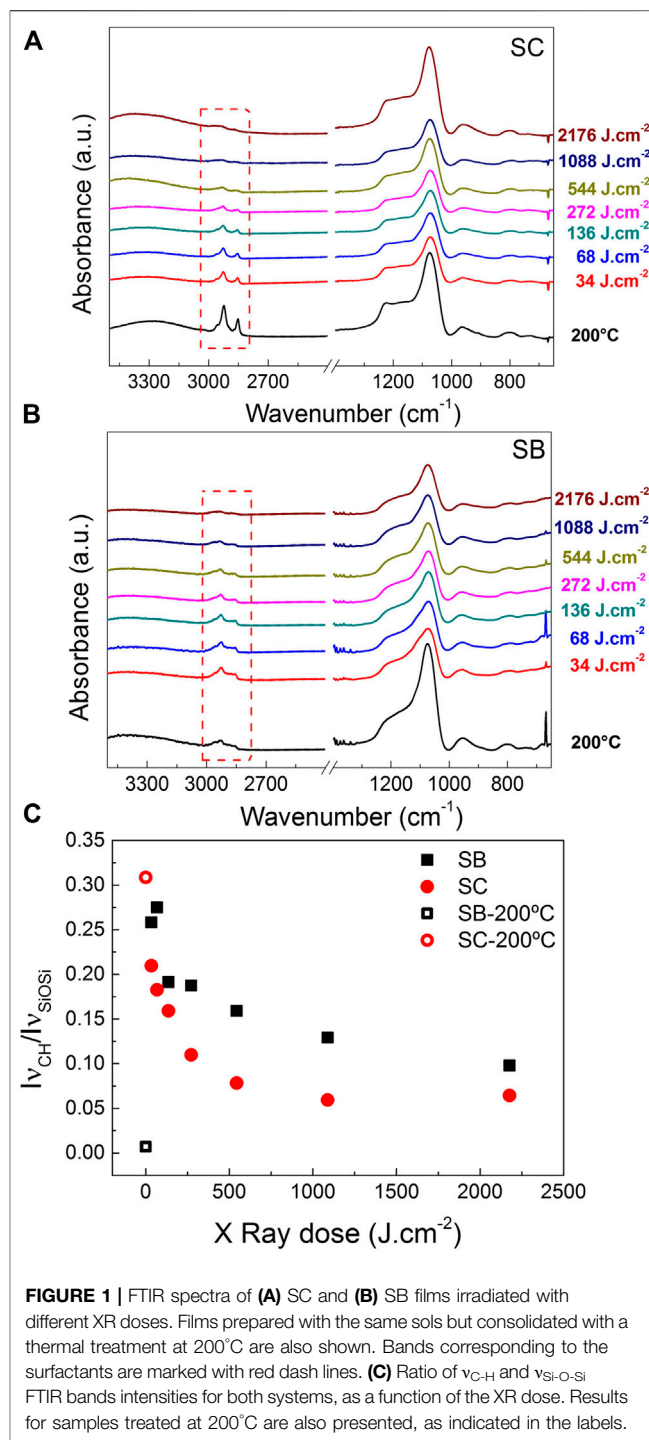
Mechanical characterization was performed using a Nano Indenter Agilent G200 equipped with a XP head and a Berkovich diamond tip. Separation distance between indents was 50 μm. Poisson's ratio ( $\nu$ ) of 0.2 was used for applying Oliver and Pharr method to SiO<sub>2</sub> films (Fischer-Cripps, 2011). More details related to these measurements are included in the **Supplementary Information**.

X-ray reflectometry (XRR) measurements were made with a Panalytical Empyrean diffractometer, using Cu K $\alpha$  radiation (1.54 Å), a 0.38 mm divergence slit and a 10 mm mask. A monochromator was positioned between the sample and the detector. The same equipment and experimental setup were used to measure X-ray diffraction (XRD) patterns in the 1.8–3°2 $\theta$  region. The critical angle and the diffraction peak corresponding to the arrangement of mesopores were both determined at around 0% and 100% relative humidity (RH) to calculate the accessible porous volume of the samples and estimate the rigidity of the films walls between pores (Dourdain and Gibaud, 2005; Gibaud et al., 2006; Klotz et al., 2006).

## RESULTS AND DISCUSSION

### Oxide Formation and Surfactant Degradation

X-ray irradiation of sol-gel films produces multiple effects depending on their composition (Innocenzi et al., 2014), including the decomposition and depolymerization of the



organic template due to bond cleavage. This effect has already been demonstrated for block-copolymers like Pluronic F127 (Innocenzi et al., 2010) and PS-b-PLA (Faustini et al., 2010). When the surfactant is part of a sol, radicals are formed in the matrix, due to the intrinsic residual humidity and to the presence of OH groups in the sample. Free radicals promote the densification of the inorganic matrix, but also enhance the degradation of the organic surfactants. Thus, the template-

oxide interaction may also have an influence on the way the XR degrade the template (Chemin et al., 2006).

FTIR measurements were conducted on irradiated SC and SB samples in order to confirm both oxide formation and surfactant degradation. These results are presented in **Figure 1**, along with the ones obtained for similar films thermally treated at 200°C. All the samples in each system were deposited using the same experimental conditions, and thus contained the same amount of precursor sol. Therefore, the comparison among FTIR spectra is straightforward.

Silicon dioxide formation is evidenced by the presence of Si-O-Si related bands located in the 1200-800  $\text{cm}^{-1}$  region (Falcaro et al., 2005). The main band is asymmetrical, with a maximum located at  $\sim 1075 \text{ cm}^{-1}$  accompanied by a defined shoulder at higher wavenumbers. Such definition in this spectral region is only observed when  $\text{SiO}_2$  is formed. In fact, it has been shown in the literature that the FTIR spectrum of the as deposited film presents a single broad band in the same region (Malfatti et al., 2011). Thus, since all the obtained spectra exhibit these defined bands, it can be assured that the oxide is formed, even in the case of the lowest XR dose explored ( $34 \text{ J}\cdot\text{cm}^{-2}$ ).

Regarding to the template, C-H bands related to the surfactants appear in the range from 3000 to 2850  $\text{cm}^{-1}$  (see enclosed area with red dash lines in **Figure 1** and the complete FTIR spectra of the templates in **Supplementary Figure S7**). It can be seen that CTAB is not degraded at 200°C (usually, temperatures around 300°C are required to completely eliminate it (Fuertes, 2009)) but it can be almost completely degraded by using an XR dose of  $544 \text{ J}\cdot\text{cm}^{-2}$  or higher. In the case of SB, the surfactant degradation is almost complete only for the highest dose studied.

For a more detailed analysis, the ratio between the  $\nu_{\text{CH}}$  band at 2926  $\text{cm}^{-1}$  and the  $\nu_{\text{SiOSi}}$  band at 1072  $\text{cm}^{-1}$  was calculated; these results are shown in **Figure 1C**. For the sake of comparison, SB-200°C and SC-200°C were also analyzed, presenting ratios equal to 0.007 and 0.3, respectively. For SC system, this ratio is much higher for the sample treated at 200°C than for the irradiated ones, confirming that this thermal treatment does not achieve the same grade of surfactant degradation as XR exposure. For SB system, this ratio is much lower for the sample treated at 200°C than for the irradiated samples, implying that the surfactant degradation with the XR is not as efficient as with thermal treatments, even at low temperatures (total degradation of Brij 58 occurs at temperatures above 250–300°C (Soler-Illia and Innocenzi, 2006; Fuertes, 2009)). These differences can be related with the dissimilarity in the chemical structure and/or molecular weight of the two templates.

The obtained tendencies regarding the influence of the XR dose (i.e., higher degradation for higher doses) were previously observed for mesoporous  $\text{SiO}_2$  templated with the triblock copolymer Pluronic F127 (Malfatti et al., 2011). At lower doses, when more hydroxyls and water are present, the degradation effect is higher, as evidenced by the decrease of the CH bands for both SB and SC systems. Afterward, as hydroxyls and water content decrease, the percentage of degradation is not increasing much even for high doses (Malfatti et al., 2015). The asymptotic level of degradation

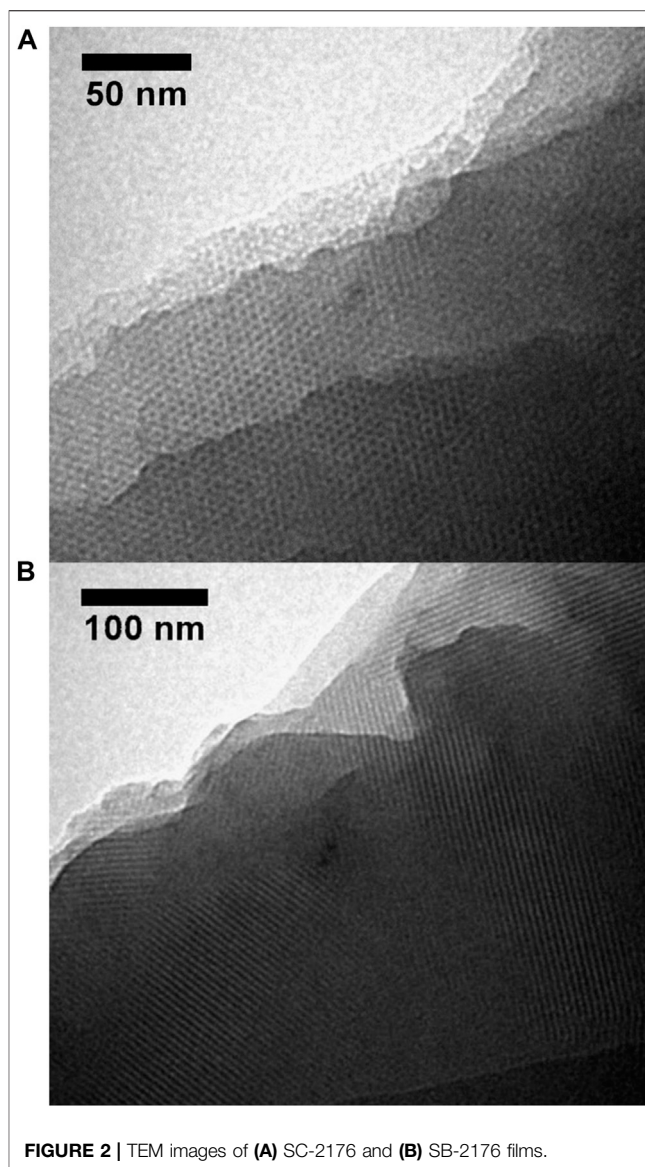


**FIGURE 2 |** TEM images of (A) SC-2176 and (B) SB-2176 films.

reached by the different surfactants depends on their composition and molecular weight. Other effects may also be involved, like X-ray ablation, photoelectron generation or Compton effect (Innocenzi et al., 2012) but they go beyond the scope of the present work.

### Pore Structure and Films Contraction

The mesoporous arrays for both SC and SB irradiated films were determined by TEM and GI-SAXS. TEM images of SC-2176 and SB-2176 samples can be seen in **Figure 2**, images of the samples obtained by thermal treatment are presented, for comparison, in **Supplementary Figure S1**. Irradiated samples exhibit large domains of ordered pores, seen as light gray areas, surrounded by the oxide walls, seen as dark gray areas. The characteristic ordering of the pores depends, as expected, on the template. In the case of CTAB (**Figure 2A**), pores are arranged following a 3D hexagonal structure ( $P6_3/mmc$ ) (Besson et al., 2000; Nicole et al.,

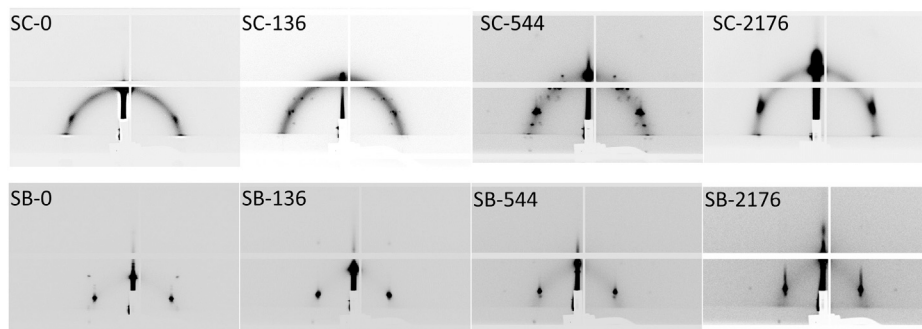


**FIGURE 3** | GI-SAXS patterns obtained for the as-prepared film (SC-0 and SB-0) and for selected irradiated films in SC (**upper row**) and SB (**lower row**) systems.

2005) while an array compatible with a body centered cubic phase ( $Im3m$ ) is obtained for Brij 58 (Angelomé et al., 2006) (**Figure 2B**). From these patterns, the inter-pore distances were calculated, resulting ( $5.1 \pm 0.5$ ) nm for SC-2176 sample and ( $5.6 \pm 0.7$ ) nm for SB-2176 sample. The obtained pore arrays and inter-pore distances values are in agreement with the ones reported for mesoporous  $SiO_2$  obtained with traditional procedures using thermal treatments (Grosso et al., 2004; Angelomé et al., 2012). As a result, it can be concluded that surfactants micelles organization and sizes are not strongly affected by XR irradiation.

GI-SAXS images for both mesostructured systems were obtained for the as-prepared films and for the irradiated and calcined films, to evaluate the meso-order and the degree of contraction. The results are concisely presented in **Figure 3** and in more detail in **Supplementary Figure S2** (SC system), **Supplementary Figure S3** (SB system) and **Supplementary Figure S4** (thermally treated systems). Clear diffraction patterns, seen as an array of points at defined distances, were found for both systems at all explored doses. This fact indicates that a high degree of 3D meso-order is present in all cases.

The different diffraction patterns observed in SC system (assigned to  $Pm3m$  and  $P6_3/mmc$  structures) are in concordance with the structures reported for CTAB templated mesoporous  $SiO_2$  (Besson et al., 2000; Grosso et al., 2002; Grosso et al., 2004) and with the structure observed by TEM for the higher dose sample. In regard to thermally treated samples, the inter-conversion between both phases as well as their coexistence are due to slight changes in the film composition during evaporation and consolidation processes as demonstrated by (Grosso et al., 2002; Grosso et al., 2004). Remarkably, a similar behavior is shown by samples exposed to XR. For SB films, an  $Im3m$  pore array was obtained for all studied doses, verifying the results obtained with TEM. This is the pore structure usually found for this oxide-template system (Angelomé et al., 2006).

The variation of the pore structure contraction (measured from the GI-SAXS patterns) and the films thicknesses (measured by ellipsometry) with the applied XR dose are presented in **Figure 4**.

The initial thicknesses of the films (i.e., after deposition and before the irradiation) are around 400 nm for SC samples and

around 250 nm for SB samples. In both systems, the thickness decreases when the XR dose is incremented, as was observed for other irradiated oxides such as ZnO (Malfatti et al., 2015),  $SiO_2$  (Innocenzi et al., 2011), hybrid  $SiO_2$  (Costacurta et al., 2010; Innocenzi et al., 2011; Jiang et al., 2016) and F127 templated mesoporous  $SiO_2$  (Malfatti et al., 2011). The macroscopical thickness reduction is accompanied by the uniaxial contraction of the pore structure in the direction perpendicular to the substrate, indicating that both effects are correlated (Lionello et al., 2017). The contraction process starts immediately after the thin film deposition, due to solvent evaporation, and continues during the following processing, due to the condensation of the oxide walls and the partial degradation of the template. These last two processes can be induced either by the irradiation or by calcination.

At first glance, from **Figure 4** observation, it can be seen that the structure contraction is more notorious when higher irradiation doses are used. However, the obtained contraction values for XR treated samples are less than 27% in all cases, even for films irradiated at  $2176 J.cm^{-2}$ . The rate of thickness change and pore structure contraction is greater at lower doses for both systems, and from a  $300 J.cm^{-2}$  dose, the changes are less noticeable. This fact can indicate that a significant degree of consolidation of the silica matrix has been produced at the lowest dose, as was also seen from the FTIR results.

Calcined films were also studied to evaluate the differences in the contraction degree between films consolidated with XR and temperature. The contraction values calculated from the SAXS patterns (**Supplementary Figure S4**) are included in **Figure 4**. It is clear that films irradiated with all studied doses contract less than calcined films: on average, the contraction of irradiated samples (around 20%) in both systems is about half of the contraction reached for films calcined at  $300^\circ C$ . This fact has important consequences for the mechanical and sorption properties, as will be shown in following sections.

It can also be observed that doses higher than  $2000 J.cm^{-2}$  generate an additional contraction and thickness reduction, which is more pronounced in SB films. This fact could be related with the surfactant degradation previously seen with FTIR (**Figure 1**). Further experiments at higher doses were then performed to obtain a more contracted structure without using additional thermal treatments. It was found that doses

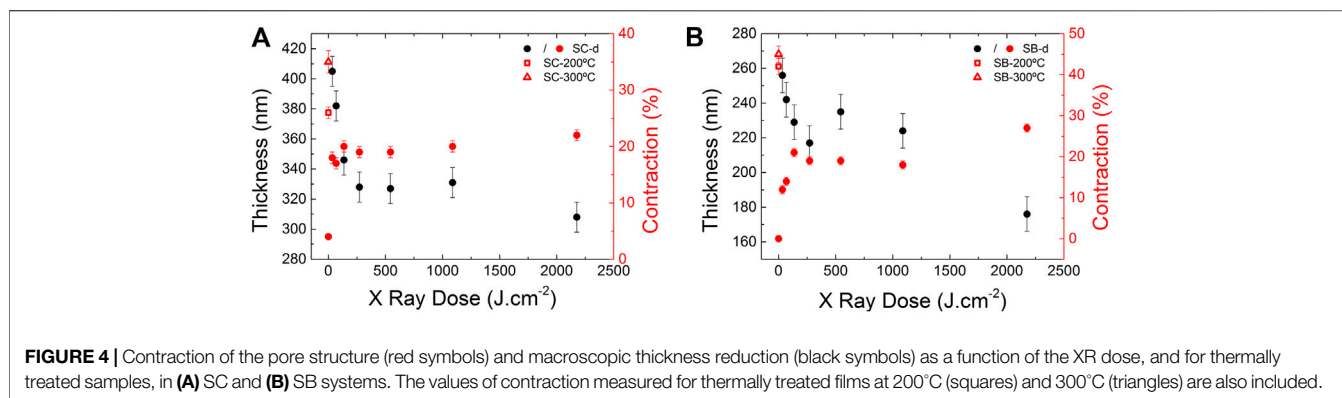


**FIGURE 4** | Contraction of the pore structure (red symbols) and macroscopic thickness reduction (black symbols) as a function of the XR dose, and for thermally treated samples, in **(A)** SC and **(B)** SB systems. The values of contraction measured for thermally treated films at 200°C (squares) and 300°C (triangles) are also included.

around 14500 J.cm<sup>-2</sup> are necessary to achieve similar contractions in both systems and, consequently, a pore interconnectivity as the one obtained for calcined films (**Supplementary Figure S5**).

### Accessible Porosity

One of the structural parameters of major importance for applications in nanofluidics and sensors is the porosity. Pores interconnectivity and surfactant elimination are necessary to achieve accessible porosity (P).

The porosity accessible to water vapor of irradiated films was determined using XRR, as described in the experimental section; an example of the measurements is presented in **Supplementary Figure S6**. For SB and SC irradiated films, a value of P around 0% was measured in almost all samples. The only exception was SC-2176; for this sample, the measured P was (15 ± 2)%. This value is lower than the usual porosity reached in this system calcined at 300°C (which is around 35–45%).

To increase the P of irradiated films, different thermal treatments and solvent rinsing for surfactant removal were explored. SB-68 and SB-136 samples were selected to accomplish this study, as they were found to be the best candidates for obtaining well-developed patterns using DXRL. Firstly, the irradiated films were rinsed in absolute ethanol for 24 and 48 h; a procedure usually applied in films consolidated at 200°C to remove the surfactant residues from inside the pores (Dourdain and Gibaud, 2005; Escobar et al., 2017). Then, films were rinsed with the same solvent and dried at 130°C. After 48 h, residues of the surfactant were still detectable by FTIR, as can be seen in **Supplementary Figure S6**. This fact could be related with the previously observed lack of contraction, which does not permit an extensive percolation of the pore system and hinders the surfactant removal. In addition, these poorly consolidated samples were macroscopically damaged during the extraction process. Hence, the immersion in ethanol, which usually works for porogen removal in non-irradiated films, is not a suitable method to eliminate the surfactant in these low-dose irradiated oxides.

In a previous work carried out with titania mesoporous films, it was found that a thermal treatment at 450°C was necessary to eliminate surfactant residues and open the pores in order to have accessible porosity (Faustini et al., 2011). Then, a thermal

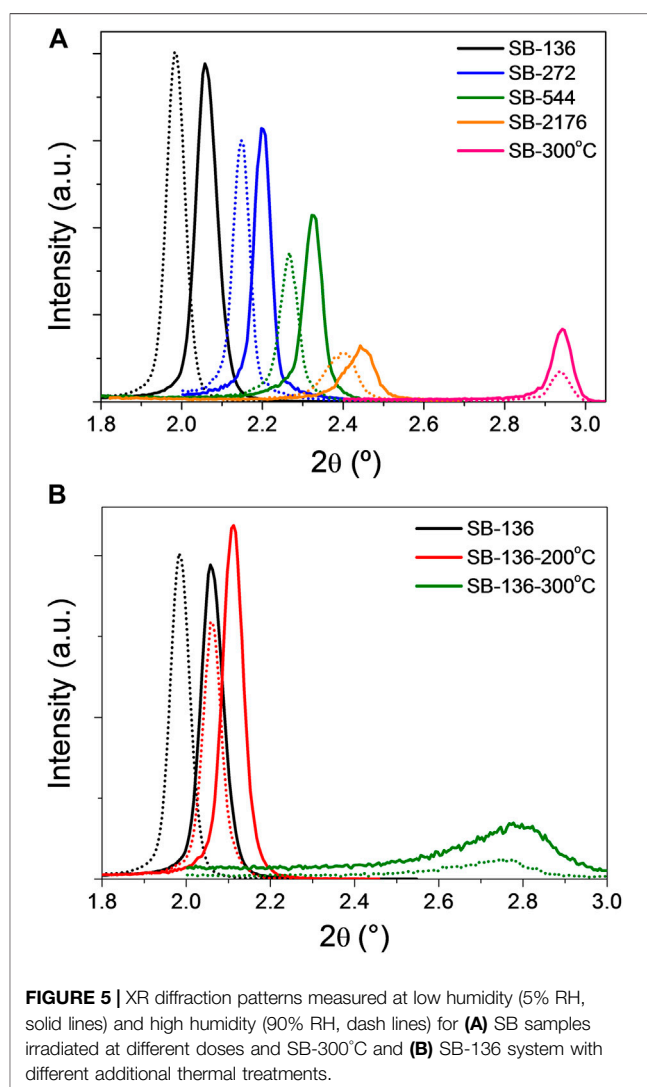


**FIGURE 5** | XRD diffraction patterns measured at low humidity (5% RH, solid lines) and high humidity (90% RH, dash lines) for **(A)** SB samples irradiated at different doses and SB-300°C and **(B)** SB-136 system with different additional thermal treatments.

treatment was explored in these silica systems to both eliminate the surfactant and open the porosity. The FTIR results are also shown in **Supplementary Figure S8**. It was found that the treatment at 200°C, even if it is followed by an extraction procedure, does not allow the fully removal of the

surfactant. However, the treatment at 300°C eliminates the template, as the contraction and pore interconnection rise. In fact, after this treatment, the  $P$  reaches values of 21–31%, depending on the initial XR dose. An example of such behavior is presented in **Supplementary Figure S6**, where the change in the critical angle of SB-136 system after the thermal treatment is shown. Thus, the thermal treatment at 300°C after irradiation is a suitable method to open the porosity in these systems.

Additional experiments were performed in the SB irradiated films to evaluate the water intrusion into the non-consolidated structure and the oxide stiffness. This template-oxide system was selected for the same reason established before, related to the ease of patterning using XR. The sample SB-300°C ( $P = (42 \pm 2)\%$ ) was also measured for comparison purposes. The XR diffraction patterns presented in **Figure 5** exhibit Bragg peaks corresponding to the planes of mesopores parallel to the substrate (Dourdain and Gibaud, 2005). The Bragg peak position measured for irradiated samples varies remarkably when the RH is changed, as can be seen in **Figure 5A**. The peak moves toward lower angles when the humidity rises, indicating that the mesostructure is swelling in the direction perpendicular to the substrate. In these samples, there are no measurable changes in the critical angle with the humidity because the intruded water is not replacing air inside the pores, which would generate a noticeable change in the film electronic density, but probably entering in the interfaces between the oxide and the template micelles and/or inside the unconsolidated oxide. The electronic densities of not-fully condensed silica and water are in the same order; for this reason, the critical angle does not significantly change when the water enters into the film. For the well consolidated porous oxide SB-300°C, the Bragg peak position does not change with the humidity as water is entering inside the empty pores. The change in Bragg peaks position with humidity diminishes with the dose, from  $0.075^\circ 2\theta$  for SB-136 up to  $0.05^\circ 2\theta$  for SB-2176, indicating a rise in the oxide stiffness. For the highly consolidated film SB-300°C, the variation with the humidity is just  $0.005^\circ 2\theta$ .

Finally, the same experiment was performed on SB-136-200°C and SB-136-300°C samples; the results are shown in **Figure 5B**. It is observed that, after the treatment at 200°C, there is still no measurable  $P$  but the Bragg peak displacement when increasing the humidity changes from  $0.075^\circ 2\theta$  for SB-136 to  $0.050^\circ 2\theta$  for SB-136-200°C, indicating an increment in the oxide stiffness. After the treatment at 300°C, the mesopore order is still present, as indicated by the existence of the Bragg diffraction peak. Besides, the  $P$  rises to  $(28 \pm 1)\%$  (**Supplementary Figure S6**) and the Bragg peak displacement diminishes to  $0.025^\circ 2\theta$ . In conclusion, a thermal treatment at 300°C performed on SB samples irradiated with a low XR dose allows obtaining a film with ordered mesopores, accessible porosity and consolidated oxide walls.

## Mechanical Properties

After the findings related to the films stiffness, indentation elastic modulus ( $E$ ) and hardness ( $H$ ) were measured using nanoindentation for SC and SB samples. Some representative

load vs. displacement curves are shown in **Supplementary Figure S9**. The measured curves do not present discontinuities or pop-ins in all studied cases, indicating that fracture or delamination events are not taking place in these supported samples (Fischer-Cripps, 2011). This is the first indication of the high toughness of these irradiated films.

$E$  and  $H$  values were calculated from the nanoindentation curves. The results obtained as a function of the XR dose are plotted in **Figure 6**, compared with the values measured for the thermally treated samples.

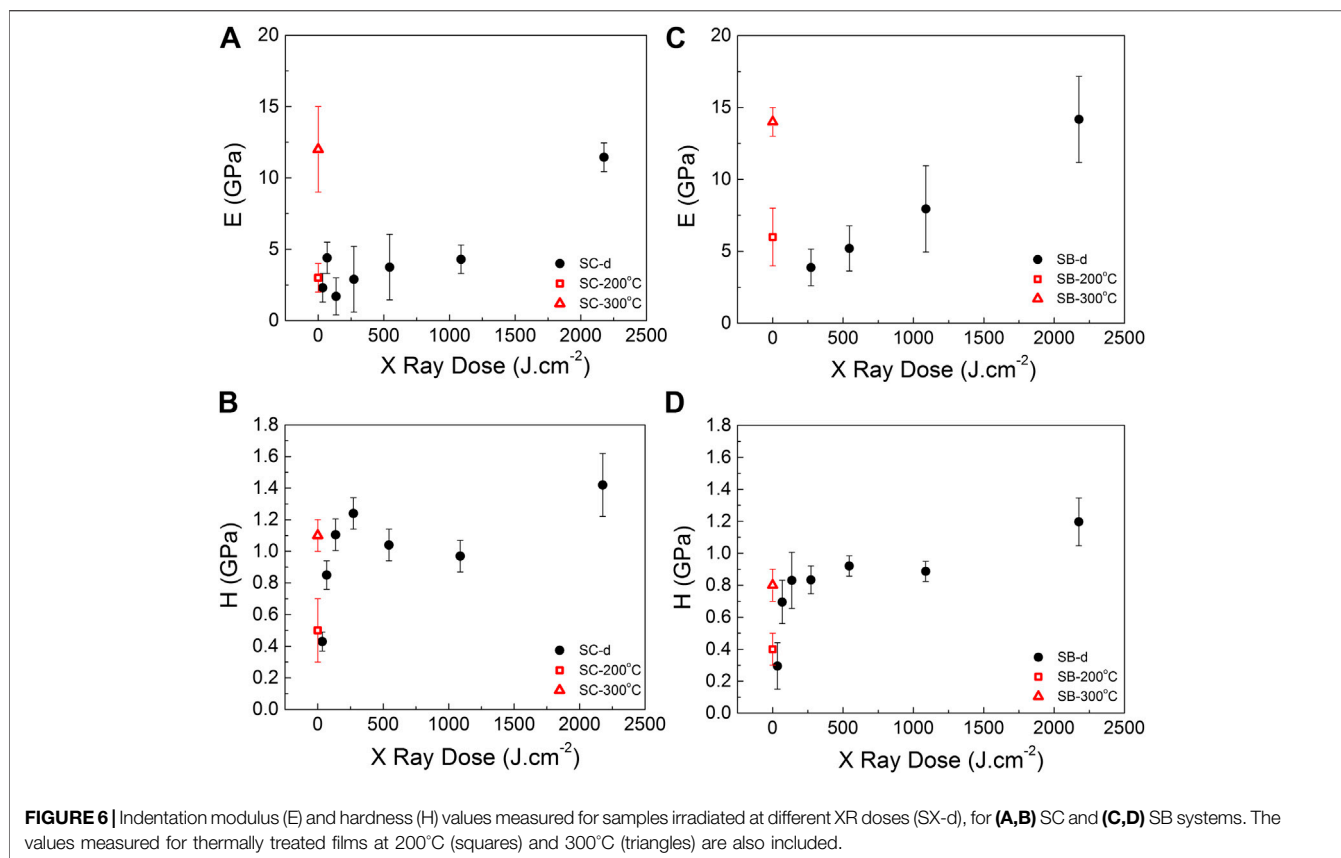
For both systems,  $E$  and  $H$  rise with the applied XR dose. The densification effect of the irradiation on the silica matrix is the responsible for this behavior, which is similar to the one previously found for non-porous hybrid silica films also synthesized using hard XR irradiation (Jiang et al., 2016).

For low XR doses, the film is composed of not fully condensed silica and residues of surfactant. This is the reason for the low  $E$  values obtained in films with doses up to  $1088 \text{ J}\cdot\text{cm}^{-2}$ , which are similar values as the obtained for films treated at 200°C. In particular, it was not possible to determine  $E$  values in SB samples irradiated at very low doses. However, in both studied systems,  $E$  values measured for the highest XR dose used ( $2176 \text{ J}\cdot\text{cm}^{-2}$ ) were comparable to  $E$  values of calcined samples, (see **Figures 6A,C**). These values are also similar to the ones found in the literature for thermally treated porous systems templated with Brij 76 (Jung et al., 2005; Ha et al., 2012), CTAB (Chemin et al., 2006) and PE6800 (Chemin et al., 2006). This implies that it is possible to obtain high  $E$  values without using thermal treatments, minimizing film contraction and preserving the samples from cracking and distortion.

**Figures 6B,D** show the change in  $H$  with the dose. In particular, a stepped increase in  $H$  with the dose up to  $300 \text{ J}\cdot\text{cm}^{-2}$  is observed for both systems. This behavior is also related to the consolidation of the inorganic structure. A plateau is found for greater doses; around 1.1 GPa for SC and 0.9 GPa for SB irradiated films. These values are in the same range of samples treated at 300°C and for other calcined mesoporous silica films reported in the literature (Jung et al., 2005; Chemin et al., 2006; Ha et al., 2012).

The high  $H$  values obtained for the irradiated systems at very low doses are probably due to the low degree of contraction in comparison to the calcined films: these less contracted films present a non-distortive surface, without the micro cracks and residual tensions that are usually generated during larger contraction events. The long-range order found by GI-SAXS, TEM, and XRD studies also reflects this aspect. Besides, the amount of residual surfactant inside the mesopores could increase the toughness of the irradiated films, as they behave as hybrid materials (Mammeri et al., 2005). A slight increase in  $H$  occurs at the highest studied doses, probably correlated with the densification of the oxide walls. In particular, there is an increase in  $H$  of over 27% in SC-2176 and of 50% in SB-2176, comparing with films calcined at 300°C for each system.

Finally, for all studied samples, the  $H/E$  ratio was calculated; the values are presented in **Supplementary Figure S10**. The  $H/E$  ratio is related with the amount of strain that a coating can suffer before a permanent deformation occurs. Therefore, a higher  $H/E$



ratio indicates a better wear resistance and toughness (Leyland and Matthews, 2000). In low doses irradiated films, extremely high H/E ratios were found, reaching values of  $0.65 \pm 0.06$  for SC-136 and  $0.21 \pm 0.06$  for SB-272. These values are one order of magnitude higher than the values usually found for silica or titania (Fischer-Cripps, 2011) and similar to the values measured for a ceramic nitride (Leyland and Matthews, 2000). As the dose rises, the H/E ratio approaches toward the values measured for the calcined porous oxides ( $0.09 \pm 0.03$  for SC-300°C and  $0.06 \pm 0.02$  for SB-300°C, see **Supplementary Figure S8**).

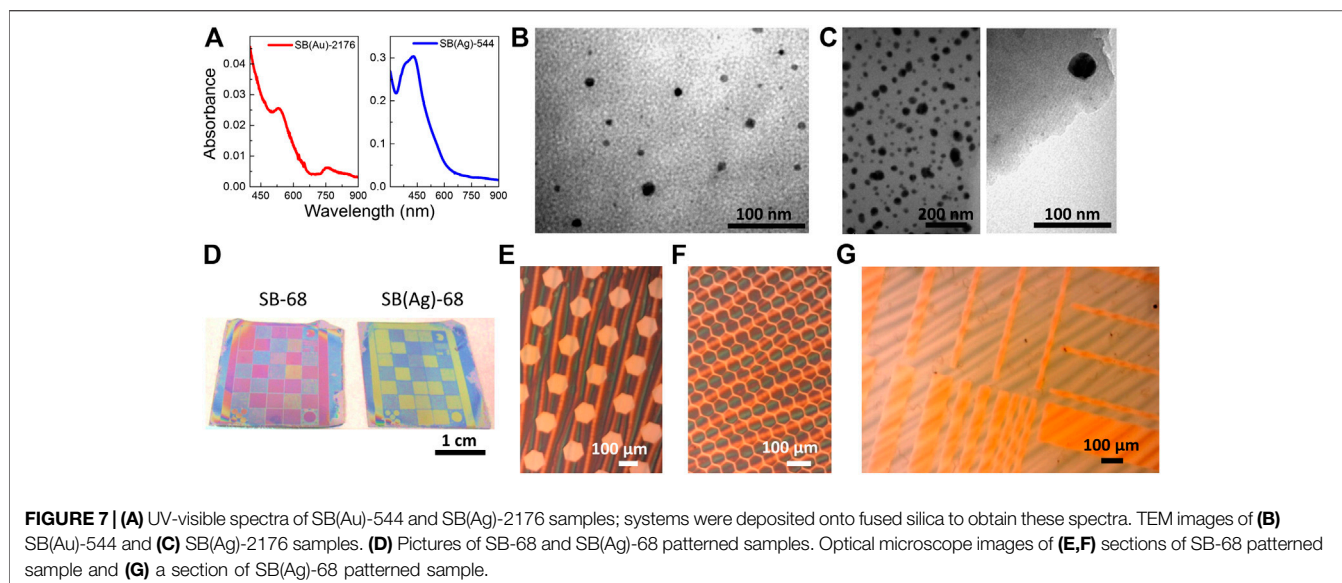
In summary, for applications that require a well-consolidated and porous oxide with good mechanical properties without the application of thermal treatments, SC irradiated at high doses is a good candidate. However, if high hardness and toughness are the required properties, hybrid SB or SC materials, irradiated at low doses, can be both good options. This irradiation at low doses can be also useful for obtaining patterned structures, with the porosity opened in a second step by using thermal treatments or an adequate solvent extraction.

## Applications

One of the main advantages of treating mesostructured thin films with XR is the possibility to prepare, in a single step, hierarchical and multifunctional materials, whose characteristics make them useful in a wide variety of applications. In this work, and for the first time to the best of our knowledge, the possibility of obtaining these advanced materials using Brij 58 templated silica was evaluated.

In a first approach, SB films were combined with metallic nanoparticles (NPs) in order to expand their potential applications for the production of sensing devices and catalysts. Two different combinations were explored: 1) architectures in which the NPs are formed during the XR exposure and 2) architectures in which the NPs were immobilized on the substrate surface prior to SB film deposition and irradiation.

For type 1) architectures,  $\text{HAuCl}_4$  or  $\text{AgNO}_3$  were included in the SB sol in order to obtain Au or Ag NPs, respectively. This approach has been used before to obtain Au and Ag loaded mesoporous  $\text{SiO}_2$ , templated with Pluronic F127 (Malfatti et al., 2010; Malfatti et al., 2011). In SB samples, for the case of gold, after a XR dose of  $2176 \text{ J.cm}^{-2}$ , the sample color changed from colorless to pink-red, typical of the presence of metallic Au NPs. The UV-visible spectrum (**Figure 7A**) reinforces this observation: a broad plasmonic band, characteristic of localized surface plasmon resonance of metallic nanoparticles, is observed (Liz-Marzán, 2004). This band presents a maximum absorption at 530 nm, as expected for spherical-like Au NPs. Additionally, TEM images (**Figure 7B**) confirm the presence of Au NPs homogeneously distributed in the oxide matrix. A broad NPs size distribution was obtained with an average diameter of  $(9 \pm 3) \text{ nm}$  (see **Supplementary Figure S11**). On the other hand, when a Ag salt was included in the sol, after a XR dose of  $544 \text{ J.cm}^{-2}$  the system presented a broad absorption band, centered around 410 nm (**Figure 7A**). This plasmonic band corresponds to the



presence of metallic Ag NPs, confirmed by TEM images, where black spherical features (i.e., the Ag NPs) distributed all around the mesoporous structure can be observed (**Figure 7C**). The obtained NPs present a broad size distribution, as shown in **Supplementary Figure S11**, in which two populations can be distinguished. The NPs of the first group present an average diameter of  $(16 \pm 6)$  nm and are included in the oxide matrix, distributed homogeneously throughout the film. A second population, consisting of larger NPs with a diameter of  $(36 \pm 8)$  nm appears to be deposited at the film surface; and even NPs ordered in lines can be distinguished. The amount of Ag NPs obtained is clearly greater than in the case of Au NPs, because a higher concentration of Ag(I) salt was included within the original sol.

These preliminary results indicate that both Au and Ag NPs can be included within the structure of SB films. Moreover, the Ag loaded system could be used for the SERS based detection of a probe molecule (*p*-nitrothiophenol). The obtained spectra, shown in **Supplementary Figure S12**, demonstrate that this molecule can diffuse through the composite and reach the Ag NP surface to be detected. Moreover, a very regular signal distribution is observed, in agreement with previous results obtained for thermally treated composites (Zalduendo et al., 2018). However, some bands attributed to Brij 58 and its degradation products are also observed in the spectra, in accordance with FTIR results shown in **Figure 1**. Thus, further experiments are required to improve the system accessibility and to tune the metallic loading.

Type (2) architectures, on the other hand, have been previously tested for the production of selective and highly sensitive SERS based sensors (López-Puente et al., 2013; López-Puente et al., 2015; Zalduendo et al., 2018; Steinberg et al., 2019). When these systems are prepared, a clear limitation appears: anisotropic NPs, the ones that present the higher SERS activity, go through a reshaping process when a thermal treatment is applied (Vanrompay et al.,

2018; Cho et al., 2020). This has been observed, for example, for Au nanostars covered with SC films, that turn into spheres after being treated at temperatures as low as 60°C (Angelomé et al., 2012). Thus, when anisotropic NPs are used, their morphology (responsible for their interesting properties) cannot be guaranteed if thermal treatments are to be used. Since there is no significant temperature increase during XR irradiation, the preparation of type (2) architectures using anisotropic Au NPs (gold triangles and gold rods) was tested. The obtained results are presented in **Supplementary Figure S13**. Firstly, the Au NPs deposited onto fused silica were irradiated with XR (dose =  $1821 \text{ J}\cdot\text{cm}^{-2}$ ). No spectral changes were observed after irradiation, indicating that the NPs are stable under these conditions. When the SB film was deposited on top and the films were treated with the same XR dose, only a shift in the spectra toward higher wavelength is observed due to the increase of the refractive index around the NPs (because of replacing air with porous  $\text{SiO}_2$  (Angelomé and Liz-Marzán, 2010)). The shape of the spectra remains unaltered, indicating that no significant NPs reshaping was produced. Hence, XR consolidated SB mesoporous thin films can be successfully combined with anisotropic Au NPs. More experiments are under way to evaluate the obtained systems as SERS based sensors.

The second approach toward the applications of SB films in the production of devices involves the use of DXRL. After exposure to XR, the unexposed sections of a mesoporous thin film can be easily etched from the substrate leaving well defined and sharp patterns. This approach was demonstrated before for a wide variety of mesoporous oxides and templates (Innocenzi et al., 2012; Marmiroli and Amenitsch, 2012; Innocenzi et al., 2014), but was not presented for SB systems. Thus, sols to obtain SB and SB(Ag) films were deposited onto silicon substrates and exposed to XR using a test mask that includes several patterns with a wide variety of sizes and shapes. After exposure, the structure was developed using different solvents and mixtures of them. Several

doses and developing solutions were tested in order to obtain adequately patterned mesoporous films. **Figure 7D** shows digital images of the samples obtained using the optimal irradiation and development conditions. The patterns can be observed by naked eye as differences of interference colors. A more detailed view of these samples, observed by optical microscopy, is presented in **Figures 7E,F** for pure SiO<sub>2</sub> and in **Figure 7G** for the Ag NPs loaded oxide. In both cases, it is possible to observe the developed pattern. For SB-68 sample, both hexagonally shaped pillars and holes are clearly observed, while for SB(Ag)-68 sample, rectangular pillars with different sizes can be seen. Interestingly, the formation of Ag NPs does not alter the lithographic process, and the presence of the particles can be noticed from the color difference observed when comparing with pure SB films. In this point, it is important to highlight that the patterns were obtained using relatively low doses, since the test experiments performed using higher doses gave rise to structures that could not be adequately developed. Thus, taking into account the results presented in the previous sections, an additional thermal treatment would be required if completely consolidated silica walls are needed together with fully accessible open porosity.

In summary, these results confirmed that XR treated SB films can be patterned and combined with metal NPs to obtain composite systems of different compositions.

## CONCLUSION

An improved strategy, combining XR irradiation with post-thermal treatments, to obtain well-consolidated, robust and accessible mesoporous silica films templated with CTAB or Brij 58 and devices derived from them, was presented in this work. By using a wide variety of characterization techniques, several aspects of the effect of XR irradiation over the two studied mesostructured films were evaluated and compared.

TEM and GI-SAXS measurements revealed that the pore ordering of these systems is not affected by the XR dose used. FTIR measurements, on the other hand, proved that a significant degree of consolidation of the silica matrix is produced even at very low XR doses. For CTAB-templated silica, the surfactant degradation with the XR is evident but for Brij 58-templated films, an extra thermal treatment at 300°C is necessary to eliminate the organic components.

Ellipsometry measurements and GI-SAXS patterns analysis demonstrated that the macroscopic and mesoscopic contractions are smaller for irradiated films, in comparison with thermally treated ones. Interestingly, while the treatment with XR generates highly ordered mesostructured and non-distorted crack free films, there is no accessible porosity in these irradiated films. Thus, to open such porosity, the efficiency of using a thermal treatment on irradiated samples was demonstrated. This thermal treatment is required not only to degrade completely the organic templates but also to interconnect the mesopores due to macroscopic film contraction. In the future, the effect of the use of solvent mixtures immediately after the XR exposure will be evaluated, in order to achieve at least partial pore accessibility by solvent extraction, without the use of temperature.

Water intrusion measurements, followed by XR diffraction, allowed determining that the films stiffness increased with the XR dose as the inorganic matrix consolidates. From the measured nanoindentation curves, it was determined that neither fracture nor delamination from the substrate occurred at the applied loads. Moreover, the indentation elastic modulus values were lower than the obtained for calcined films due to the presence of a not fully condensed oxide matrix and surfactant residues inside the pores. On the other hand, high hardness values were obtained even at low doses, probably due to the presence of surfactant and to the less contracted structure, in comparison to thermally treated films. The combination of high hardness with low modulus obtained at low doses makes these films excellent candidates for applications where a surface with high wear resistance is required.

The knowledge of the structural and mechanical parameters of irradiated mesoporous silica films will allow the design of the synthesis strategy to integrate these materials in several devices. Achieving accessible porosity will be particularly useful for this purpose. As a first approach in this way, the possibility of combining SB films with Ag and Au metallic nanoparticles in several architectures and the use of DXRL to obtain patterned films was demonstrated. These results open new possibilities in the development of sensors, catalysts and nano and microfluidic devices with biomedical, nanoelectronics and nanoionics applications, among others. In fact, new kind of lab-on-a-chip devices with tailored areas that can be selectively functionalized for manipulation of biological substances like proteins can be envisioned.

## DATA AVAILABILITY STATEMENT

The original contributions presented in the study are included in the article/**Supplementary Material**, further inquiries can be directed to the corresponding authors.

## AUTHOR CONTRIBUTIONS

PS participated in the synthesis, FTIR and SAXS studies. DL performed the mechanical studies. DM participated in the XRR and FTIR studies. MZ participated in the synthesis, the acquisition of TEM images and the optical characterization. HA participated in the measurements of SAXS patterns. LG helped with the XRR studies. BM participated in the films synthesis and lithography. PA and MF directed the project and participated in the synthesis and characterization. All authors participated in the manuscript writing process.

## ACKNOWLEDGMENTS

The authors acknowledge the CERIC-ERIC Consortium for the access to experimental facilities and financial support (projects 20177003 and 20157040). This work includes part of the scientific activities of the internal CERIC-ERIC project Renewals. ANPCyT (PICT 2015-0351 and 2017-1133) partially funded this work. The authors thank to A. Fasciszewski, J. Bonaparte and D. Rodríguez

for the access to the Clean Room (CAC, CNEA) and the help with the ellipsometer operation, and G. Zbihlei (CAC, CNEA) for the TEM images. PS, DL, and MZ acknowledge CONICET for their doctoral fellowships and DEMA acknowledges Instituto Sabato for her master fellowship.

## REFERENCES

- Amenitsch, H., Bernstorff, S., Kriechbaum, M., Lombardo, D., Mio, H., Rappolt, M., et al. (1997). Performance and first results of the ELETTRA high-flux beamline for small-angle X-ray scattering. *J. Appl. Crystallogr.* 30 (5), 872–876. doi:10.1107/S0021889897001593
- Angelomé, P. C., and Fuertes, M. C. (2018). “Metal nanoparticles-mesoporous oxide nanocomposite thin films,” in *Handbook of sol-gel science and technology*. Editors L. Klein, M. Aparicio, and A. Jitianu (Cham: Springer International Publishing), 2507–2533.
- Angelomé, P. C., and Liz-Marzán, L. M. (2010). Monitoring solvent evaporation from thin films by localized surface plasmon resonance shifts. *J. Phys. Chem. C* 114 (43), 18379–18383. doi:10.1021/jp106528n
- Angelomé, P. C., and Liz-Marzán, L. M. (2014). Synthesis and applications of mesoporous nanocomposites containing metal nanoparticles. *J. Sol. Gel Sci. Technol.* 70 (2), 180–190. doi:10.1007/s10971-013-3238-8
- Angelomé, P. C., Fuertes, M. C., and Soler-Illia, G. J. A. A. (2006). Multifunctional, multilayer, multiscale: integrative synthesis of complex macro and mesoporous thin films with spatial separation of porosity and function. *Adv. Mater.* 18, 2397–2402. doi:10.1002/adma.200600439
- Angelomé, P. C., Pastoriza-Santos, I., Pérez Juste, J., Rodríguez-González, B., Zelcer, A., Soler-Illia, G. J. A. A., et al. (2012). Growth and branching of gold nanoparticles through mesoporous silica thin films. *Nanoscale* 4, 931–939. doi:10.1039/c2nr11547f
- Besson, S., Ricolleau, C., Gacoin, T., Jacquiod, C., and Boilot, J. P. (2000). A new 3D organization of mesopores in oriented CTAB silica films. *J. Phys. Chem. B* 104 (51), 12095–12097. doi:10.1021/jp0026538
- Brinker, C. J., Lu, Y., Sellinger, A., and Fan, H. (1999). Evaporation-induced self-assembly: nanostructures made easy. *Adv. Mater.* 11 (7), 579–585. doi:10.1002/(sici)1521-4095(199905)11:7<579::aid-adma579>3.0.co;2-r
- Cerrina, F. (2000). X-ray imaging: applications to patterning and lithography. *J. Phys. Appl. Phys.* 33 (12), R103–R116. doi:10.1088/0022-3727/33/12/201
- Chemin, N., Klotz, M., Rouessac, V., Ayrat, A., and Barthel, E. (2006). Mechanical properties of mesoporous silica thin films: effect of the surfactant removal processes. *Thin Solid Films* 495 (1), 210–213. doi:10.1016/j.tsf.2005.08.260
- Cho, H., Shin, J. W., and Ryoo, R. (2020). Atomic scale mechanisms underlying thermal reshaping of anisotropic gold nanocrystals revealed by *in Situ* electron microscopy. *J. Phys. Chem. C* 124 (23), 12855–12863. doi:10.1021/acs.jpcc.0c04281
- Costacurta, S., Malfatti, L., Patelli, A., Falcaro, P., Amenitsch, H., Marmiroli, B., et al. (2010). Deep X-ray lithography for direct patterning of PECVD films. *Plasma Process. Polym.* 7 (6), 459–465. doi:10.1002/ppap.200900147
- Doherty, C. M., Gao, Y., Marmiroli, B., Amenitsch, H., Lisi, F., Malfatti, L., et al. (2012). Microfabrication of mesoporous silica encapsulated enzymes using deep X-ray lithography. *J. Mater. Chem.* 22 (32), 16191–16195. doi:10.1039/C2JM32863A
- Dourdain, S., and Gibaud, A. (2005). On the capillary condensation of water in mesoporous silica films measured by x-ray reflectivity. *Appl. Phys. Lett.* 87 (22), 223105. doi:10.1063/1.2136412
- Dubois, G., Volksen, W., Magbitang, T., Sherwood, M. H., Miller, R. D., Gage, D. M., et al. (2008). Superior mechanical properties of dense and porous organic/inorganic hybrid thin films. *J. Sol. Gel Sci. Technol.* 48 (1), 187–193. doi:10.1007/s10971-008-1776-2
- Escobar, A., Yate, L., Grzelczak, M., Amenitsch, H., Moya, S. E., Bordoni, A. V., et al. (2017). One-step synthesis of mesoporous silica thin films containing available COOH groups. *ACS Omega* 2 (8), 4548–4555. doi:10.1021/acsomega.7b00560
- Etienne, M., Quach, A., Grosso, D., Nicole, L., Sanchez, C., and Walcarius, A. (2007). Molecular transport into mesostructured silica thin films: electrochemical monitoring and comparison between p6m, P63/mmc, and Pm3n structures. *Chem. Mater.* 19 (4), 844–856. doi:10.1021/cm0625068
- Falcaro, P., Costacurta, S., Malfatti, L., Buso, D., Patelli, A., Schiavuta, P., et al. (2011). Chemical tailoring of hybrid sol–gel thick coatings as hosting matrix for functional patterned microstructures. *ACS Appl. Mater. Interfaces* 3 (2), 245–251. doi:10.1021/am100901m
- Falcaro, P., Costacurta, S., Malfatti, L., Takahashi, M., Kidchob, T., Casula, M. F., et al. (2008). Fabrication of mesoporous functionalized arrays by integrating deep X-ray lithography with Dip-Pen writing. *Adv. Mater.* 20 (10), 1864–1869. doi:10.1002/adma.200702795
- Falcaro, P., Costacurta, S., Mattei, G., Amenitsch, H., Marcelli, A., Guidi, M. C., et al. (2005). Highly ordered “defect-free” self-assembled hybrid films with a tetragonal mesostructure. *J. Am. Chem. Soc.* 127 (11), 3838–3846. doi:10.1021/ja0427956
- Falcaro, P., Malfatti, L., Vaccari, L., Amenitsch, H., Marmiroli, B., Greci, G., et al. (2009). Fabrication of advanced functional devices combining soft chemistry with X-ray lithography in one step. *Adv. Mater.* 21 (48), 4932–4936. doi:10.1002/adma.200901561
- Fan, H., Hartshorn, C., Buchheit, T., Tallant, D., Assink, R., Simpson, R., et al. (2007). Modulus–density scaling behaviour and framework architecture of nanoporous self-assembled silicas. *Nat. Mater.* 6 (6), 418–423. doi:10.1038/nmat1913
- Faustini, M., Marmiroli, B., Malfatti, L., Louis, B., Krins, N., Falcaro, P., et al. (2011). Direct nano-in-micropatterning of TiO<sub>2</sub> thin layers and TiO<sub>2</sub>/Pt nanoelectrode arrays by deep X-ray lithography. *J. Mater. Chem.* 21 (11), 3597–3603. doi:10.1039/c0jm03493b
- Faustini, M., Vayer, M., Marmiroli, B., Hillmyer, M., Amenitsch, H., Sinturel, C., et al. (2010). Bottom-up approach toward titanosilicate mesoporous pillared planar nanochannels for nanofluidic applications. *Chem. Mater.* 22 (20), 5687–5694. doi:10.1021/cm101502n
- Fischer-Cripps, A. C. (2011). *Nanoindentation*. New York: Springer-Verlag. doi:10.1007/978-1-4757-5943-3
- Fuertes, M. C. (2009). *Materiales funcionales multiescala basados en películas de óxidos mesoporosos*. PhD Thesis. San Martín, Argentina: Universidad de San Martín.
- Fuertes, M. C., Colodrero, S., Lozano, G., González-Elipe, A. R., Grosso, D., Boissière, C., et al. (2008). Sorption properties of mesoporous multilayer thin films. *J. Phys. Chem. C* 112 (9), 3157–3163. doi:10.1021/jp710612y
- Fuertes, M. C., López-Alcaraz, F. J., Marchi, M. C., Troiani, H. E., Luca, V., Míguez, H., et al. (2007). Photonic crystals from ordered mesoporous thin-film functional building blocks. *Adv. Funct. Mater.* 17 (8), 1247–1254. doi:10.1002/adfm.200601190
- Gibaud, A., Dourdain, S., and Vignaud, G. (2006). Analysis of mesoporous thin films by X-ray reflectivity, optical reflectivity and grazing incidence small angle X-ray scattering. *Appl. Surf. Sci.* 253, 3–11. doi:10.1016/j.apsusc.2006.05.121
- Giménez, G., Ybarra, G., and Soler-Illia, G. J. A. A. (2020). Preparation of mesoporous silica thin films at low temperature: a comparison of mild structure consolidation and template extraction procedures. *J. Sol. Gel Sci. Technol.* 96 (2), 287–296. doi:10.1007/s10971-020-05410-z
- Gonzalez Solveyra, E., Fuertes, M. C., Soler-Illia, G. J. A. A., and Angelomé, P. C. (2017). 2D-SAXS *in situ* measurements as a tool to study elusive mesoporous phases: the case of p6mm TiO<sub>2</sub>. *J. Phys. Chem. C* 121 (6), 3623–3631. doi:10.1021/acs.jpcc.6b12112
- Grosso, D., Babonneau, F., Albouy, P.-A., Amenitsch, H., Balkenende, A. R., Brunet-Bruneau, A., et al. (2002). An *in situ* study of mesostructured CTAB–silica film formation during Dip coating using time-resolved SAXS and interferometry measurements. *Chem. Mater.* 14 (2), 931–939. doi:10.1021/cm011255u
- Grosso, D., Balkenende, A. R., Albouy, P. A., Lavergne, M., Mazerolles, L., and Babonneau, F. (2000). Highly oriented 3D-hexagonal silica thin films produced

## SUPPLEMENTARY MATERIAL

The Supplementary Material for this article can be found online at: <https://www.frontiersin.org/articles/10.3389/fmats.2021.628245/full#supplementary-material>.

- with cetyltrimethylammonium bromide. *J. Mater. Chem.* 10 (9), 2085–2089. doi:10.1039/B003178J
- Grosso, D., Cagnol, F., Soler-Illia, G. J. A. A., Crepaldi, E. L., Amenitsch, H., Brunet-Bruneau, A., et al. (2004). Fundamentals of mesostructuring through evaporation-induced self-assembly. *Adv. Funct. Mater.* 14 (4), 309–322. doi:10.1002/adfm.200305036
- Ha, T.-J., Park, H.-H., Jang, H. W., Yoon, S.-J., Shin, S., and Cho, H. H. (2012). Study on the thermal stability of ordered mesoporous SiO<sub>2</sub> film for thermal insulating film. *Microporous Mesoporous Mater.* 158, 123–128. doi:10.1016/j.micromeso.2012.03.028
- Innocenzi, P., and Malfatti, L. (2013). Mesoporous thin films: properties and applications. *Chem. Soc. Rev.* 42 (9), 4198–4216. doi:10.1039/c3cs35377j
- Innocenzi, P., Kidchob, T., Costacurta, S., Falcaro, P., Marmiroli, B., Cacho-Nerin, F., et al. (2010). Patterning block copolymer thin films by deep X-ray lithography. *Soft Matter* 6 (14), 3172–3176. doi:10.1039/B925105G
- Innocenzi, P., Malfatti, L., and Falcaro, P. (2012). Hard X-rays meet soft matter: when bottom-up and top-down get along well. *Soft Matter* 8 (14), 3722–3729. doi:10.1039/C2SM07028F
- Innocenzi, P., Malfatti, L., Kidchob, T., Costacurta, S., Falcaro, P., Marmiroli, B., et al. (2011). Densification of sol-gel silica thin films induced by hard X-rays generated by synchrotron radiation. *J. Synchrotron Radiat.* 18 (2), 280–286. doi:10.1107/S0909049510051666
- Innocenzi, P., Malfatti, L., Marmiroli, B., and Falcaro, P. (2014). Hard X-rays and soft-matter: processing of sol-gel films from a top down route. *J. Sol. Gel Sci. Technol.* 70 (2), 236–244. doi:10.1007/s10971-013-3227-y
- Jiang, Y., Carboni, D., Pinna, A., Marmiroli, B., Malfatti, L., and Innocenzi, P. (2016). Hard X-rays for processing hybrid organic-inorganic thick films. *J. Synchrotron Radiat.* 23 (1), 267–273. doi:10.1107/s1600577515018597
- Jung, S.-B., Han, C.-K., and Park, H.-H. (2005). Electrical and mechanical properties of surfactant-templated mesoporous silica thin films using Brij-76 surfactant. *Appl. Surf. Sci.* 244 (1), 47–50. doi:10.1016/j.apsusc.2004.09.127
- Klotz, L., Rouessac, V., Rébiscoul, D., Ayrat, A., and van der Lee, A. (2006). Adsorption-desorption isotherms of nanoporous thin films measured by X-ray reflectometry. *Thin Solid Films* 495, 214–218. doi:10.1016/j.tsf.2005.08.168
- López-Puente, V., Abalde-Cela, S., Angelomé, P. C., Alvarez-Puebla, R. A., and Liz-Marzán, L. M. (2013). Plasmonic mesoporous composites as molecular sieves for SERS detection. *J. Phys. Chem. Lett.* 4 (16), 2715–2720. doi:10.1021/jz4014085
- López-Puente, V., Angelomé, P. C., Soler-Illia, G. J. A. A., and Liz-Marzán, L. M. (2015). Selective SERS sensing modulated by functionalized mesoporous films. *ACS Appl. Mater. Interfaces* 7 (46), 25633–25640. doi:10.1021/acsami.5b10543
- Leyland, A., and Matthews, A. (2000). On the significance of the H/E ratio in wear control: a nanocomposite coating approach to optimised tribological behaviour. *Wear* 246 (1), 1–11. doi:10.1016/S0043-1648(00)00488-9
- Lionello, D. F., Steinberg, P. Y., Zalduendo, M. M., Soler-Illia, G. J. A. A., Angelomé, P. C., and Fuertes, M. C. (2017). Structural and mechanical evolution of mesoporous films with thermal treatment: the case of Brij 58 templated titania. *J. Phys. Chem. C* 121 (40), 22576–22586. doi:10.1021/acs.jpcc.7b09054
- Liu, N., Assink, R. A., Smarsly, B., and Brinker, C. J. (2003). Synthesis and characterization of highly ordered functional mesoporous silica thin films with positively chargeable -NH<sub>2</sub> groups. *Chem. Commun. (Camb)* (10), 1146–1147. doi:10.1039/B301910A
- Liz-Marzán, L. M. (2004). Nanometals: formation and color. *Mater. Today*, 26–31. doi:10.1016/S1369-7021(04)00080-X
- Malfatti, L., Carboni, D., Pinna, A., Lasio, B., Marmiroli, B., and Innocenzi, P. (2016). *In situ* growth of Ag nanoparticles in graphene-TiO<sub>2</sub> mesoporous films induced by hard X-ray. *J. Sol. Gel Sci. Technol.* 79 (2), 295–302. doi:10.1007/s10971-016-4052-x
- Malfatti, L., Falcaro, P., Marmiroli, B., Amenitsch, H., Piccinini, M., Falqui, A., et al. (2011). Nanocomposite mesoporous ordered films for lab-on-chip intrinsic surface enhanced Raman scattering detection. *Nanoscale* 3 (9), 3760–3766. doi:10.1039/C1NR10404G
- Malfatti, L., Marongiu, D., Costacurta, S., Falcaro, P., Amenitsch, H., Marmiroli, B., et al. (2010). Writing self-assembled mesostructured films with *in situ* formation of gold nanoparticles. *Chem. Mater.* 22 (6), 2132–2137. doi:10.1021/cm902625v
- Malfatti, L., Pinna, A., Enzo, S., Falcaro, P., Marmiroli, B., and Innocenzi, P. (2015). Tuning the phase transition of ZnO thin films through lithography: an integrated bottom-up and top-down processing. *J. Synchrotron Radiat.* 22 (1), 165–171. doi:10.1107/s1600577514024047
- Mammeri, F., Bourhis, E. L., Rozes, L., and Sanchez, C. (2005). Mechanical properties of hybrid organic-inorganic materials. *J. Mater. Chem.* 15 (35–36), 3787–3811. doi:10.1039/B507309J
- Marmiroli, B., and Amenitsch, H. (2012). X-ray lithography and small-angle X-ray scattering: a combination of techniques merging biology and materials science. *Eur. Biophys. J.* 41 (10), 851–861. doi:10.1007/s00249-012-0843-3
- Nicole, L., Boissiere, C., Grosso, D., Quach, A., and Sanchez, C. (2005). Mesostructured hybrid organic-inorganic thin films. *J. Mater. Chem.* 15 (35–36), 3598–3627. doi:10.1039/B506072A
- Pérennès, F., De Bona, F., and Pantenburg, F. J. (2001). Deep X-ray lithography beamline at ELETTRA. *Nucl. Instrum. Methods Phys. Res. Sect. A Accel. Spectrom. Detect. Assoc. Equip.* 467–468, 1274–1278. doi:10.1016/S0168-9002(01)00632-5
- Pinna, A., Lasio, B., Piccinini, M., Marmiroli, B., Amenitsch, H., Falcaro, P., et al. (2013). Combining top-down and bottom-up routes for fabrication of mesoporous titania films containing ceria nanoparticles for free radical scavenging. *ACS Appl. Mater. Interfaces* 5 (8), 3168–3175. doi:10.1021/am4001024
- Sánchez, C., Boissière, C., Grosso, D., Laberty, C., and Nicole, L. (2008). Design, synthesis, and properties of inorganic and hybrid thin films having periodically organized nanoporosity. *Chem. Mater.* 20 (3), 682–737. doi:10.1021/cm702100t
- Scarabelli, L., Coronado-Puchau, M., Giner-Casares, J. J., Langer, J., and Liz-Marzán, L. M. (2014). Monodisperse gold nanotriangles: size control, large-scale self-assembly, and performance in surface-enhanced Raman scattering. *ACS Nano* 8 (6), 5833–5842. doi:10.1021/nn500727w
- Scarabelli, L., Sánchez-Iglesias, A., Pérez-Juste, J., and Liz-Marzán, L. M. (2015). A “Tips and Tricks” practical guide to the synthesis of gold nanorods. *J. Phys. Chem. Lett.* 6 (21), 4270–4279. doi:10.1021/acs.jpcc.5b02123
- Soler-Illia, G. J. A. A., and Innocenzi, P. (2006). Mesoporous hybrid thin films: the physics and chemistry beneath. *Chem. Eur. J.* 12 (17), 4478–4494. doi:10.1002/chem.200500801
- Soler-Illia, G. J. A. A., Angelomé, P. C., Fuertes, M. C., Grosso, D., and Boissiere, C. (2012). Critical aspects in the production of periodically ordered mesoporous titania thin films. *Nanoscale* 4 (8), 2549–2566. doi:10.1039/C2NR11817C
- Steinberg, P. Y., Zalduendo, M. M., Giménez, G., Soler-Illia, G. J. A. A., and Angelomé, P. C. (2019). TiO<sub>2</sub> mesoporous thin films architecture as a tool to control Au nanoparticles growth and sensing capabilities. *Phys. Chem. Chem. Phys.* 21, 10347–10356. doi:10.1039/C9CP01896D
- Vanrompay, H., Bladt, E., Albrecht, W., Béché, A., Zakhozheva, M., Sánchez-Iglesias, A., et al. (2018). 3D characterization of heat-induced morphological changes of Au nanostars by fast *in situ* electron tomography. *Nanoscale* 10 (48), 22792–22801. doi:10.1039/C8NR08376B
- Vanstreels, K., Wu, C., Verdonck, P., and Baklanov, M. R. (2012). Intrinsic effect of porosity on mechanical and fracture properties of nanoporous ultralow-k dielectrics. *Appl. Phys. Lett.* 101 (12), 123109. doi:10.1063/1.4753972
- Wolosiuk, A., Tognalli, N. G., Martínez, E. D., Granada, M., Fuertes, M. C., Troiani, H., et al. (2014). Silver nanoparticle-mesoporous oxide nanocomposite thin films: a platform for spatially homogeneous SERS-active substrates with enhanced stability. *ACS Appl. Mater. Interfaces* 6 (7), 5263–5272. doi:10.1021/am500631f
- Xiao, X., Hata, N., Yamada, K., and Kikkawa, T. (2003). Mechanical properties of periodic porous silica low-k films determined by the twin-transducer surface acoustic wave technique. *Rev. Sci. Instrum.* 74 (10), 4539–4541. doi:10.1063/1.1611615
- Zalduendo, M. M., Langer, J., Giner-Casares, J. J., Halac, E. B., Soler-Illia, G. J. A. A., Liz-Marzán, L. M., et al. (2018). Au nanoparticles-mesoporous TiO<sub>2</sub> thin films composites as SERS sensors: a systematic performance analysis. *J. Phys. Chem. C* 122 (24), 13095–13105. doi:10.1021/acs.jpcc.8b01444
- Zhou, W., Bailey, S., Sooryakumar, R., King, S., Xu, G., Mays, E., et al. (2011). Elastic properties of porous low-k dielectric nano-films. *J. Appl. Phys.* 110 (4), 043520. doi:10.1063/1.3624583

**Conflict of Interest:** The authors declare that the research was conducted in the absence of any commercial or financial relationships that could be construed as a potential conflict of interest.

Copyright © 2021 Steinberg, Lionello, Medone Acosta, Zalduendo, Amenitsch, Granja, Marmiroli, Angelomé and Fuertes. This is an open-access article distributed under the terms of the Creative Commons Attribution License (CC BY). The use, distribution or reproduction in other forums is permitted, provided the original author(s) and the copyright owner(s) are credited and that the original publication in this journal is cited, in accordance with accepted academic practice. No use, distribution or reproduction is permitted which does not comply with these terms.